RSC Advances

PAPER

View Article Online
View Journal | View Issue



Cite this: *RSC Adv.*, 2016, **6**, 98722

# Promising field electron emission performance of vertically aligned one dimensional (1D) brookite (β) $TiO_2$ nanorods

Rupesh S. Devan,*[ab] Yuan-Ron Ma,*[c] Mahendra A. More,*[b] Ruchita T. Khare,[b] Vivek V. Antad,[d] Ranjit A. Patil,[c] Vishal P. Thakare,[be] Rajendra S. Dhayal[f] and Lukas Schmidt-Mende[g]

Received 17th August 2016
Accepted 8th October 2016

DOI: 10.1039/c6ra20747b

www.rsc.org/advances

We evidence field-electron emission (FE) studies on the large-area array of one-dimensional (1D) brookite (β) $TiO_2$ nanorods. The pure 1D β-$TiO_2$ nanorods of 10 nm width and 760 nm long were synthesized on Si substrate utilizing hot-filament metal vapor deposition technique. X-ray diffraction (XRD) and transmission electron microscopy (TEM) analysis evidenced the β-$TiO_2$ nanorods to be composed of orthorhombic crystals in brookite (β) phase. X-ray photoemission spectroscopy (XPS) revealed the formation of pure stoichiometric (*i.e.* 1 : 1.98) 1D $TiO_2$ nanorods. The values of turn-on field, required to draw current density of 10 μA $cm^{-2}$, was observed 3.9 V $\mu m^{-1}$ for pristine 1D β-$TiO_2$ nanorods emitters, which were found significantly lower than doped/undoped 1D $TiO_2$ nanostructures (*i.e.* nanotubes, nanowires, nanorods) based field emitters. The enhanced FE behavior of the $TiO_2$/Si emitter can be attributed to modulation of electronic properties due to the high aspect ratio of vertically aligned $TiO_2$ nanorods. Furthermore, the orthodox emission situation of pristine $TiO_2$/Si emitters exhibit good emission stability and reveal their potentials as promising FE material.

## Introductions

The one-dimensional (1D) nanostructure morphologies of transition metal oxides offer the advantages of a high aspect ratio, sharp tip features, good stability, and oxidation resistance,[1] which are prerequisites to enhance the field emission (FE) properties and develop efficient functional devices. Among the various 1D metal-oxides, $TiO_2$ is one of the most fascinating functional materials. It has received considerable attention for applications in solar cell,[2] photocatalysis,[3] electrochromic displays,[4] supercapacitors,[5] and batteries,[6] *etc.*, owing to its non-toxicity, abundance, and good chemical and thermal stability. The FE properties of $TiO_2$ are rather explored in spite of its low work function range (3.9 to 4.5 eV) than other popular metal-oxides, owing to its availability in limited morphological forms.[6] The geometrical similarity of $TiO_2$ nanotubes with carbon nanotubes influenced many researchers to explore the FE characteristics of $TiO_2$ nanotubes[7–10] and nanotubes with sharp tips.[11] However, the reproducibility of the $TiO_2$ nanotubes remained challenging. Not only the diameter influence the FE performance, but the density (*i.e.* separation between nanotubes) and clusters appearance of the $TiO_2$ nanotubes array appear to create field screening effects.[7] Moreover, the uncontrolled and random dispersion of $TiO_2$ nanowires[12] and nanorods[13] affect their FE adversely. Highly dense rutile $TiO_2$ hierarchical nanorods network arranged in the form of dandelion flower like morphology suffer from significant field screening effect thereby exhibiting poorer FE behavior.[14] On the contrary, the influence of oxygen vacancies on the electron affinity alter the electronic structure of $TiO_2$ and thereof FE properties.[15] Therefore, the doping of 1D $TiO_2$ nanostructures with N,[9] Fe,[16] and C,[17] *etc.* was seldom adopted to enhance the FE characteristics.

Theoretical analysis and experimental studies have proved the advantage of brookite (β) phase over anatase and rutile phase of $TiO_2$. Mo *et al.*[18] have reported electronic and optical properties of three different polymorphs (rutile, anatase, and brookite) of $TiO_2$. They used first-principles orthogonalized linear combinations of atomic orbitals (OLCAO) method to calculate the electronic structure of $TiO_2$ and reported that the brookite phase has a much larger static dielectric constant of

[a]*Centre for Physical Sciences, School of Basics and Applied Sciences, Central University of Punjab, Bathinda, 151001, India. E-mail: devan_rs@yahoo.co.in*

[b]*Department of Physics, Savitribai Phule Pune University, (Formerly, University of Pune), Pune 411007, India. E-mail: mam@physics.unipune.ac.in*

[c]*Department of Physics, National Dong Hwa University, Hualien 97401, Taiwan, Republic of China. E-mail: ronma@mail.ndhu.edu.tw*

[d]*Nowrosjee Wadia College of Arts & Science, 19, Late Prin. V. K. Joag Path, Pune 411001, India*

[e]*Physical & Materials Chemistry Division, CSIR-National Chemical Laboratory, Dr Homi Bhabha Road, Pune 411008, India*

[f]*Centre for Chemical Sciences, School of Basics and Applied Sciences, Central University of Punjab, Bathinda, 151001, India*

[g]*Department of Physics, University of Konstanz, Constance 78457, Germany*

7.89 compared to that of rutile (6.62) and anatase (6.04) phase. Furthermore, comparably better photoactivity is observed in brookite $TiO_2$ thin films/nanoparticles than the anatase and rutile.[19,20] Shibata *et al.*[21] found brookite $TiO_2$ nanoparticles as excellent coating materials because of its better photoinduced hydrophilicity than anatase one. Koelsch *et al.*[22] reported better photovoltaic abilities of brookite $TiO_2$ nanoparticles over anatase phase in terms of bandgap and electrochemical characterization in water and acetonitrile. Furthermore, our detailed report on excellent electrochromic properties with 99% reversibility[4] and highly stable supercapacitive performance with long cycle lifetime (10 000 cycles) of brookite $TiO_2$ nanoneedles[5] corroborate significant electronics advantages of the brookite phase over the anatase and rutile phase. However, the brookite consisting of distorted $TiO_6$ octahedra is less investigated. The synthesis of pure brookite phase is always challenging due to its metastable nature[23] and commonly accompanied with the anatase and/or rutile phases.[3,24,25] That is why numerous scientific reports are found on the utilization of rutile and anatase phases for variety of applications including field emitters.[10–12,26,27] High temperature calcinations[25] and annealing[24] processes were unsuccessful to yield pure brookite phase. Nevertheless, β-phase is thermodynamically most stable in nanocrystalline form at dimensions between 11–35 nm.[3] Despite the facts above, to the best of our knowledge, there is no study report on FE performance of 1D β-$TiO_2$ nanorods. Therefore, for promising FE behavior, it is of scientific and technological importance to growing vertically aligned 1D β-$TiO_2$ nanorods.

In this work, we present 1D β-$TiO_2$ nanorods arrays as promising field-emitters. The large area arrays of vertically aligned $TiO_2$ nanorods of brookite phase were synthesized using hot-filament metal vapor deposition (HF-MVD) technique, which is unique and simple technique to provide diverse nanostructures morphologies.[28–33] The structural morphology, size distribution, electronic structure, and chemical composition of as-synthesized large-area arrays β-$TiO_2$ nanorods was examined utilizing various techniques such as X-ray photoemission spectroscopy (XPS), field-emission scanning electron microscopy (FESEM), transmission electron microscope (TEM), and X-ray diffractometer (XRD), *etc.* Interestingly, the vertically aligned and uniformly distributed 1D β-$TiO_2$ nanorods array exhibit low turn-on field, good emission stability, and large field enhancement factor.

## Experimental

Large area arrays of $TiO_2$ nanorods were synthesized using hot-filament metal vapor deposition (HFMVD) technique. A clean titanium (Ti) wire (99.9% pure) of a diameter of 1 mm, passed through a pure graphite disc was fixed on two supporting Cu electrodes in a vacuum chamber. Once the pressure of the vacuum chamber was pumped down to $1.3 \times 10^{-2}$ mbar, the Ti wire was heated to ~1300 °C for 25 min to generate controlled hot titanium vapor. The hot titanium vapor encountered and reacted with the residual oxygen (or leaking air) to form a metal-oxide vapor of $TiO_x$ ($x \leq 2$). $TiO_x$ vapors meet rather cold Si wafers (substrate) which had been placed on the graphite disc holder (~3 mm above the Ti wire) and condensed into one-dimensional (1D) $TiO_2$ nanorods. After that, the surface morphology of the as-synthesized large-area arrays of β-$TiO_2$ nanorods was characterized using a field emission scanning electron microscope (FESEM, JEOL JSM-6500F). The crystal structure of β-$TiO_2$ nanorods was confirmed with an X-ray diffractometer (Philips X'Pert PRO) with Cu-Kα radiations ($\lambda$ = 1.541 Å). Structural analysis of β-$TiO_2$ nanorods was carried out using a transmission electron microscope (TEM, JEOL, JEM-2100) with a selected-area electron diffractometer (SAED) at an accelerating voltage of 200 kV. The band-structure and chemical states present in as-synthesized β-$TiO_2$ nanorods was analyzed using X-ray photoelectron spectrometer (XPS, Thermo Scientific Inc. K-alpha) with a microfocus monochromated Al Kα X-ray. The individual FE studies of the $TiO_2$ nanorods were carried out in a vacuum chamber at a base pressure of ~$10 \times 10^{-9}$ mbar. The semitransparent phosphor screen as an anode was maintained at an optimized distance from specimen/samples of β-$TiO_2$ nanorods. Moreover, to avoid the effect of contamination, preconditioning of the samples was carried out by applying a voltage of ~3 kV for 30 min. The FE current ($I$) was measured with an electrometer (Keithley 6514) at dc voltage ($V$) applied using high voltage DC power supply (0–40 kV, Spellman, U.S.). The long-term stability of the FE current was recorded for the $TiO_2$ nanorods.

## Results and discussion

The surface morphology in FESEM images (Fig. 1) reveals the formation of uniformly distributed and vertically aligned $TiO_2$ nanorods on Si substrate. Uniformly distributed $TiO_2$ nanorods over a large area (Fig. 1(a)) signifies variation in their diameters (inset of Fig. 1(a)), which were confined to the very limited range and all are smaller than 20 nm. The array contains ~2550 nanorods per square micrometer. The high magnification tilted view (Fig. 1(b)) of $TiO_2$ nanorods recorded at a tilt angle of 35° to the surface normal direction shows vertically standing and well separated nanorods with their clearly visible textural boundaries. The high magnification FESEM image in Fig. 1(c) shows a side view of the $TiO_2$ nanorods array with an average length of ~760 nm. This indicates that no distinct thin layer of $SiO_2$ or $TiO_2$ nanoparticles has formed before the growth of the $TiO_2$ nanorods even after a high temperature of the Ti source (1300 °C). A statistical histogram of the diameter distribution (Fig. 1(d)) illustrates that the diameter of the $TiO_2$ nanorods falls in the range of 5 to 20 nm. Most of the $TiO_2$ nanorods have a diameter of about ~10 nm. This distribution of varying diameters can be fitted to a log-normal distribution function as,

$$f_N(w) = \frac{A}{d\sigma\sqrt{2\pi}} \exp\left[ - \frac{\ln(d/\bar{d})^2}{2\sigma^2} \right] \quad (1)$$

where, $d$ is the diameter of the nanorods; $\bar{d}$ [≡ 10.81 ± 0.13 nm] is the mean (average) diameter of various nanorods; $A$ [≡ 93.65 ± 4.93] is the normalization constant; and $\sigma$ [≡ 0.21 ± 0.01] is the standard deviation of diameters of nanorods. The log-

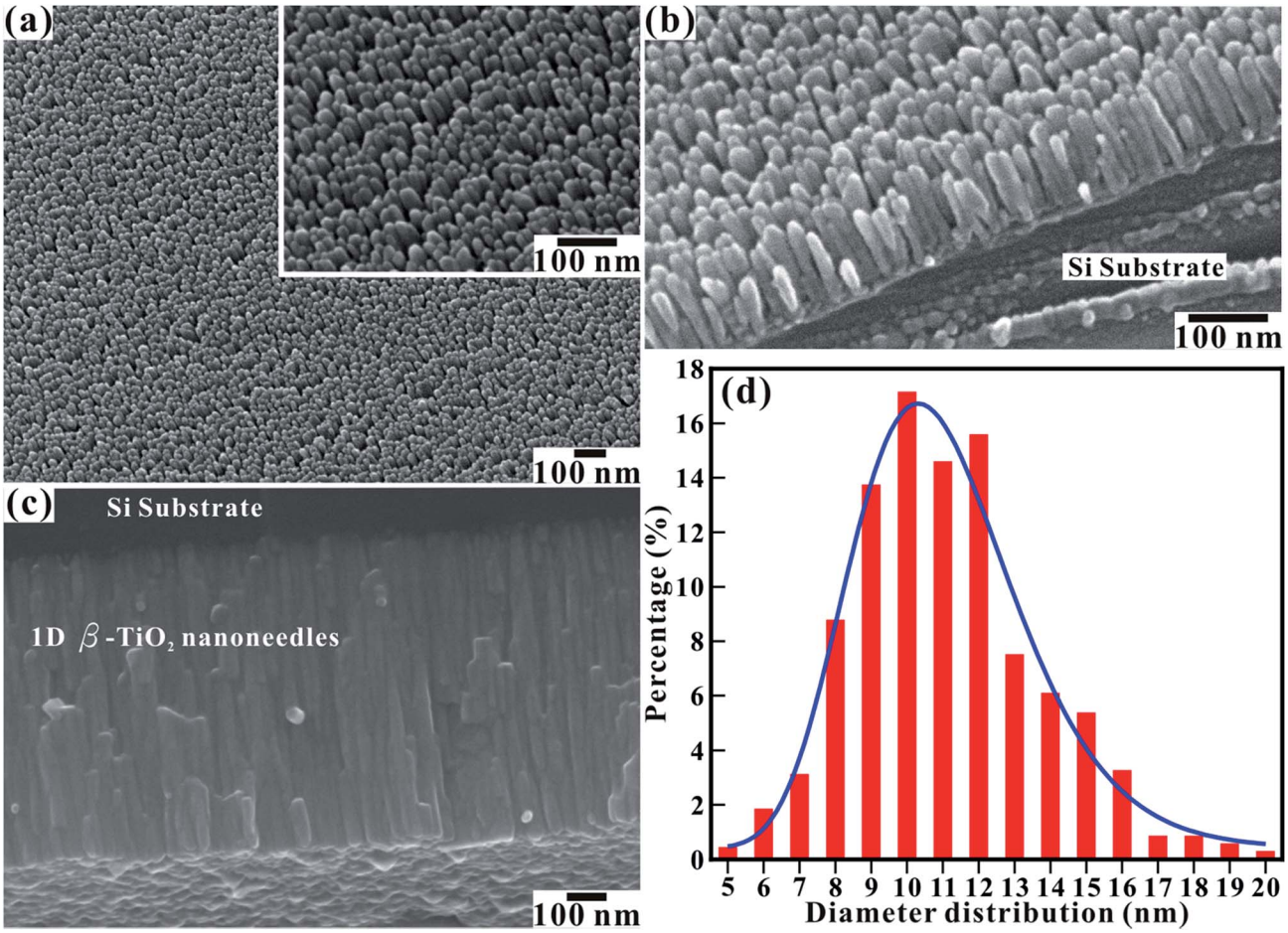


Fig. 1 FESEM image showing the (a) top, (b) tilted, and (c) side views of the large-area array of vertically aligned 1D $TiO_2$ nanorods on Si substrate. Inset of (a) shows high-magnification FESEM image of the 1D $TiO_2$ nanorods. The tilted view was recorded at a tilt angle of 35° to the surface normal direction. (d) Statistical histogram of the diameter distribution of the $TiO_2$ nanorods fitted by a log-normal distribution function.

normal distribution of diameters of the nanorods is asymmetrical. The small standard deviation ($\sigma \leq 0.25$) of the diameter distribution indicates that the nanorods are well confined to a limited diameter range.

XRD pattern is used as a fingerprint to identify the crystalline structure of the $TiO_2$ nanorods. The room temperature XRD pattern of as-synthesized $TiO_2$ nanorods arrays (Fig. 2(a)) exhibits a sets of well-defined diffraction peaks (indicated by β) at $2\theta$ values of 32.4, 37.1, 38.8, 44.8, 45.5, 46.2, 52.3, 52.9, 55.6, 57.9, 75.6, 76.6, and 77.8, respectively, are indexed to the (020), (021), (121), (212), (302), (411), (420), (222), (511), (322), (531), (432), and (423) lattice planes of orthorhombic crystals of $TiO_2$ in brookite (β) phase, assigned to the space group *Pbca* (JCPDS – 761936) with lattice constants of $a = 0.919$ nm, $b = 0.546$ nm, $c = 0.516$ nm and $\alpha = \beta = \gamma = 90°$. The remaining diffraction peaks (indicated by asterisks) represents the Si substrate in cubic crystalline form of the space group $P2_13$ with lattice contacts $a = b = c = 7.16$ nm, and $\alpha = \beta = \gamma = 90°$ (JCPDS – 850621). Further, the crystalline structure of β-$TiO_2$ nanorods was confirmed by selected area electron diffraction (SAED) pattern (Fig. 2(b)) of a β-$TiO_2$ nanorod extracted from large area array. The SAED pattern was collected from the portion of the β-$TiO_2$ nanorod shown in the inset of Fig. 2(b), which evidenced four-fold symmetric diffraction spots indexed to the [101] zone axis. The indexing of the reflections in the SAED pattern is well consistent with the XRD analysis discussed above. This clearly evidenced that the β-$TiO_2$ nanorods were indeed composed of orthorhombic crystals in brookite (β) phase. Most of the phase transformation results suggest that thermodynamic phase stability for the three polymorphs of $TiO_2$ is rutile > brookite > anatase. Kominami *et al.*[25] reported that anatase is thermodynamically stable at crystalline dimensions below 11 nm, brookite is most stable for dimensions between 11–35 nm, and rutile is stable above the 35 nm. Therefore, decisive synthesis parameters (*i.e.* temperature, time and pressure) of the HFMVD technique were optimized to achieve the diameter of $TiO_2$ nanorods below 35 nm. Therefore, dimensions of nanorods (*i.e.* <20 nm) observed in this study ruled out the possibility of formation of rutile phase. The synthesis process involving additional reactants such as water and acid/base medium assists the faster nucleation process than the growth of the morphology (*e.g.* 1D or 0D) favor for the formation of anatase phase.[8,9,11,17,34,35] Furthermore, faster nucleation process than the growth leads to the lower size morphologies. Synthesis of

 

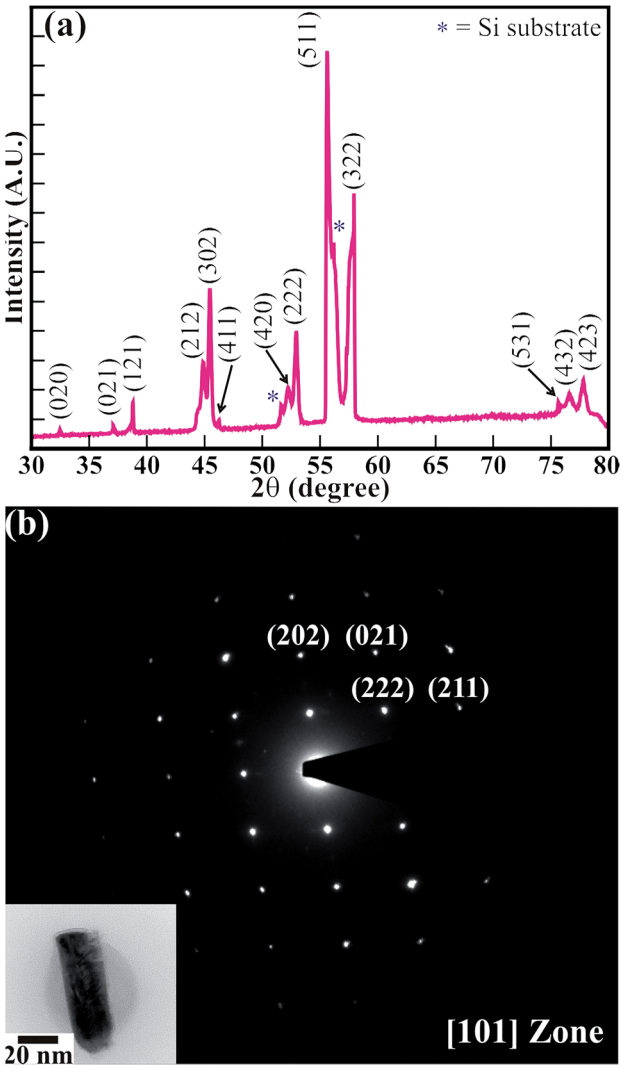


Fig. 2 (a) XRD pattern of a large area array of the 1D $TiO_2$ nanorods on Si-substrate, (b) SAED pattern collected from a single 1D $TiO_2$ nanorod shows diffraction spots indexed to the [101] zone axis of brookite crystal structure. Inset of (b) shows TEM image of single 1D $TiO_2$ nanorod extracted from the large area array.

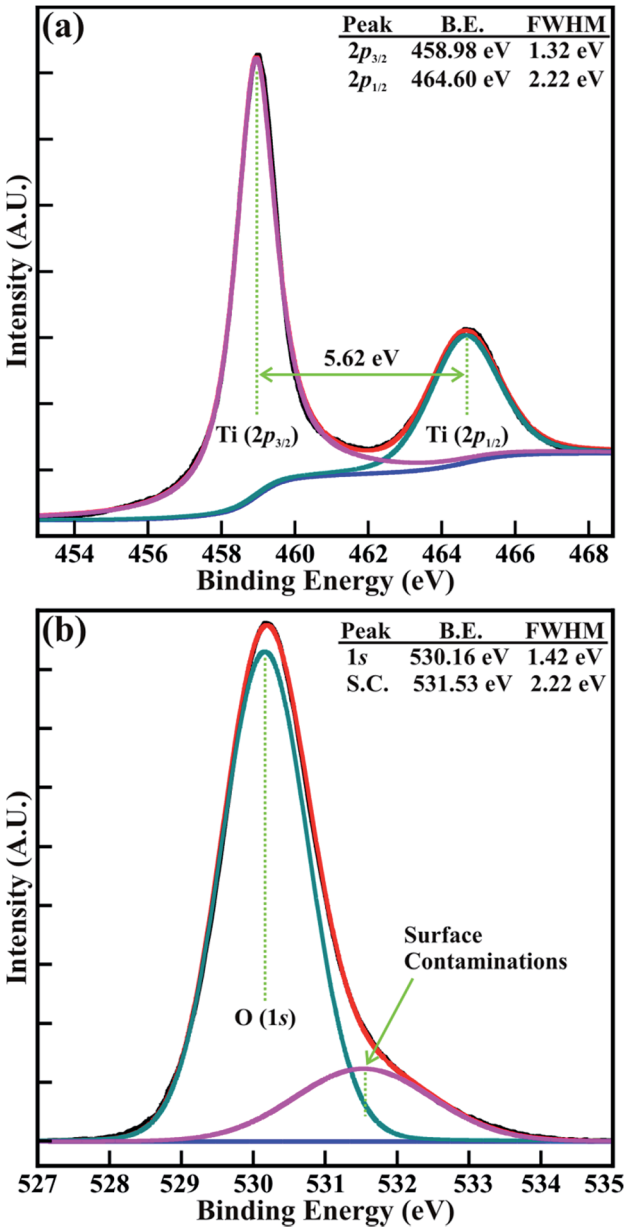


Fig. 3 Typical high-resolution XPS spectra of the (a) Ti (2p) and (b) O (1s) core levels of the large area array of 1D β-$TiO_2$ nanorods. The XPS spectra were decomposed *via* Voigt curve function fitting.

$TiO_2$ nanorods is carried out by heating Ti-metal filament at a higher temperature in the absence of additional reactants. Consequently, the formation of β-$TiO_2$ nanorods is observed, and other phases such as anatase and rutile have been precluded.

XPS studies were carried out for the quantitative analysis of the electronic structure and chemical properties of β-$TiO_2$ nanorods. To precisely determine the features of the double peaks of Ti ($2p_{3/2}$) and Ti ($2p_{1/2}$), the Ti (2p) XPS spectra was decomposed *via* Voigt curve fitting within the Shirley background (Fig. 3(a)). The perfect fit for two peaks located at binding energies (BE) of 458.98 and 464.60 eV, respectively, corresponds to the Ti ($2p_{3/2}$) and Ti ($2p_{1/2}$) core levels of $Ti^{4+}$ cations and not of $Ti^{3+}$.[36,37] The energy separation of 5.62 eV between Ti ($2p_{3/2}$) and Ti ($2p_{1/2}$) peaks and their area ratio of 2.49 reflects a strong bonding between Ti and O atoms. The full width at half maximum (FWHM) of the Ti ($2p_{3/2}$) and Ti ($2p_{1/2}$) peak are 1.32 and 2.22, respectively, indicative of the high resolution of the Ti (2p) XPS spectrum in comparison with previous studies.[37,38] Similarly, O (1s) XPS spectra of nanorods was decomposed *via* Voigt curve fitting within the Shirley background (Fig. 3(b)). The results demonstrate the perfect fits to two peaks located at 530.16 and 531.53 eV, with FWHM's of 1.42 and 2.22 eV, respectively. The lower BE peak at 530.14 eV corresponds to the O (1s) core level of the $O^{2-}$ anions in β-$TiO_2$ nanorods. However, higher BE at 531.53 eV is ascribed to surface contamination, such as carbon oxides or hydroxides.[39–41] The O (1s) peak observed at BE of 530.16 eV, is associated with the Ti–O chemical bonding ($O_{1s}^{Ti-O}$).[36] The atomic

ratio of oxygen and titanium (*i.e.* O/Ti) estimated by integrating the area beneath the decomposed peaks of O (1s) and Ti ($2p_{3/2}$) is ~1.98 (*i.e.* Ti : O = 1 : 1.98), which is very close to the stoichiometric ratio (*i.e.* 1 : 2) of pure $TiO_2$. This confirms that all nanorods in the large area array are fully oxidized, and composed of pure stoichiometric $TiO_2$ only and no titanium suboxides ($TiO_x$). Moreover, the BE difference ($\Delta E$) of 71.18 eV between O (1s) and Ti ($2p_{3/2}$) peaks is very close to that of 71.5 eV for $TiO_2$, and significantly smaller than that of 73.4 eV for $Ti_2O_3$ and 75.0 eV for TiO.[42] This confirms again that, nanorods array is formed of pure stoichiometric $TiO_2$.

FE measurements of pristine β-$TiO_2$ nanorods (≡ 1D β-$TiO_2$/Si) were performed in a planar diode configuration. The macroscopic area of the emitting device was ~0.30 $cm^2$, and values of the anode–cathode separation used were 500, 1000, 1500 and 2000 μm. The variation in the macroscopic electron emission current density ($J$) as a function of applied electric field ($E$) shown in Fig. 4(a). In this work, the applied field $E$ is defined by $E = V/d_{sep}$, where $V$ is the voltage applied between electrodes separated by a distance $d_{sep}$. This field $E$ is not uniform in our apparatus but is a form of the average field between the electrodes. The emission current increased rapidly with the gradual increase in applied voltage. Interestingly, the larger emission current density of ~470 μA $cm^{-2}$ was drawn at an applied field of 6 V $\mu m^{-1}$ for the anode–cathode separation of 2000 μm. When the separation increases from 500 to 2000 μm, the turn-on ($E_{on}$) field required to extract emission current density of 10 μA $cm^{-2}$, is decreased steadily from 5.6 to 3.9 V $\mu m^{-1}$. These values of $E_{on}$ are much lower than that reported for anodically fabricated $TiO_2$ nanotip arrays of anatase and rutile phases (*i.e.* 8.6 to 10.8 V $\mu m^{-1}$),[11] free-standing $TiO_2$ nanotube arrays with ridged structures (*i.e.* 34 V $\mu m^{-1}$),[2] thermally evaporated single-crystalline $TiO_2$ nanowires (5.7 V $\mu m^{-1}$), pristine $TiO_2$ nanotube arrays (18.86 V $\mu m^{-1}$),[43] carbon-doped $TiO_2$ nanotube array (5.0 V $\mu m^{-1}$),[44] rutile $TiO_2$ nanorods annealed at high temperatures (3.96–7.46 V $\mu m^{-1}$),[13] $TiO_2$ nanotubes/nanowires of differentiated heights (7.5/6.7 V $\mu m^{-1}$),[35] $TiO_2$ nanoflowers composed of nanoneedles (4.76 V $\mu m^{-1}$),[45] and 3D microsphere (4.07 V $\mu m^{-1}$) of rutile $TiO_2$.[46] The $E_{on}$ of β-$TiO_2$ nanorods is analogous to hydrothermally synthesized quasi-microsphere carrying urchin-like $TiO_2$ nanostructures of rutile phase (3.81 V $\mu m^{-1}$).[46] Furthermore, 1D β-$TiO_2$ nanorods achieved lower $E_{on}$ than the $TiO_2$ nanotubes anodized in ethylene glycol electrolyte with 2 and 15 vol% $H_2O$ content (8.8 and 9.1 V $\mu m^{-1}$, respectively) which was reduced with a further increase in the vol% of $H_2O$ content,[47] but the specific reasons in support of this reduction are unknown yet. Moreover, the $E_{on}$ of β-$TiO_2$ nanorods is more promising than that obtained from hydrothermally synthesized ZnO nanotubes (7.0 V $\mu m^{-1}$) at current density of 0.1 μA $cm^{-2}$.[48] Relatively lower $E_{on}$ reported for ZnO nanocombs (3.6 V $\mu m^{-1}$) and Ni-doped ZnO nanowires (3.21 V $\mu m^{-1}$) is achieved at current density of 1 μA $cm^{-2}$ and 0.1 μA $cm^{-2}$, respectively.[49,50] Furthermore, β-$TiO_2$ nanorods produced larger emission current density than electrodeposited ZnO nanosheets (50.1 μA $cm^{-2}$) at an applied field of 6.4 V $\mu m^{-1}$, respectively.[51] The threshold field ($E_{thr}$) correspond to the current density of 100 μA $cm^{-2}$ was 7, 5.8, 5 and 4.8 V $\mu m^{-1}$, for

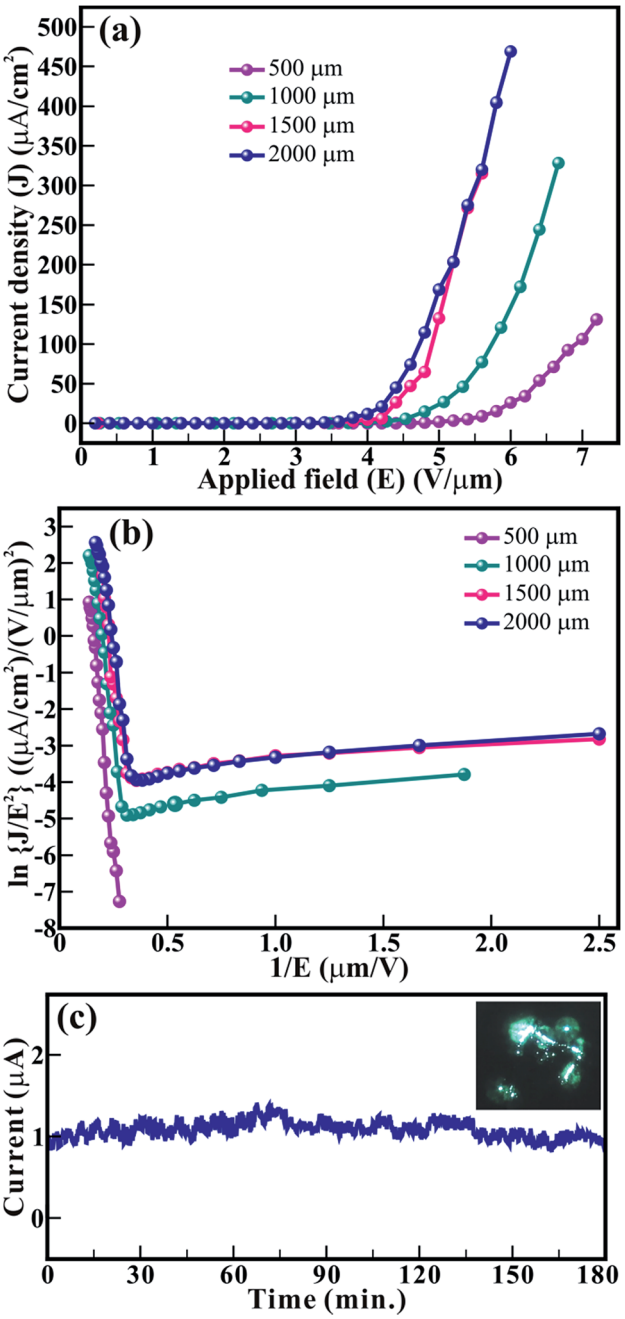


Fig. 4 Field emission (a) $J$–$E$ curves of a large area array of vertically aligned 1D β-$TiO_2$ nanorods measured at different vacuum separations (*i.e.* 500, 1000, 1500 and 2000 μm) and their corresponding (b) F–N plots indicating the emission current from the semiconducting emitters. (c) Field emission current stability ($I$–$t$) plot of 1D β-$TiO_2$ nanorods.

the separations of 500, 1000, 1500, and 2000 μm, respectively. This decrease in threshold field with increasing anode–cathode separation is somewhat surprising. For a well defined array of silicon nanotip emitters, similar behavior, was observed by Cheng *et al.*,[52] and claimed that, for a very short anode–cathode distance, where the potential barrier seek by an electron tunneling through a vacuum gap has increased dramatically; and an electron either require more energy or a large applied

 

Table 1 The scaled-barrier-field ($f$) values for β-$TiO_2$/Si emitters obtained using spreadsheet provided by 'Forbes' in the ref. 55

| Separation (μm) | $f_{low}$ | $f_{high}$ | Orthodoxy test result | Remarks |
|---|---|---|---|---|
| 500 | 0.26 | 0.47 | Pass | — |
| 1000 | 0.30 | 0.55 | Apparently reasonable | Two highest-field points excluded |
| 1500 | 0.29 | 0.47 | Pass | — |
| 2000 | 0.30 | 0.49 | Pass | One highest-field point excluded |



field to tunnel through the potential barrier compared with electron emission at large anode–cathode distance. Therefore, except for the electrostatic screening effect depending on the emitter's density and sharpness, the vacuum gap is also important when considering the effect of potential barrier on the transport of electrons.

A modified Fowler–Nordheim (F–N) equation, used to express the emission current density and electric field relationship of semiconducting nanostructures is as follows,[53]

$$J = \alpha_f a \Phi^{-1} E^2 \beta^2 \exp\left( - \frac{b\Phi^{3/2}}{\beta E} \nu_F \right) \quad (2)$$

where, $J$ is the device average FE current density, $\alpha_f$ is a macroscopic pre-exponential correction factor, $a$ and $b$ are constants ($a = 1.54 \times 10^{-6}$ A eV $V^{-2}$, $b = 6.83089 \times 10^3$ $eV^{-3/2}$ V $\mu m^{-1}$), $\Phi$ is the work function of the emitter (*i.e.* 4.3 eV for $TiO_2$), $E$ is the applied average electric field, $\beta$ is the local electric field enhancement factor, and $\nu_F$ is a particular value of the principal Schottky–Nordheim barrier function $\nu$ (correction factor). The emitter surface for the 1D nanostructures deposited over a larger area is treated to be rough. Therefore, the applied and local electric field differs from each other at the emission sites, and their ratio is known as the field enhancement factor ($\beta$). The eqn (2) is further analyzed by plotting a graph of $\ln\{J/E^2\}$ *versus* $(1/E)$, known as Fowler–Nordheim (F–N) plot. In an approach compatible with eqn (2), the field enhancement factor ($\beta$) is determined from the value of $\Phi$ and the slope $S$ of this FN plot, by using the equation.

$$\beta = \frac{-sb\Phi^{3/2}}{S} \quad (3)$$

where, $s$ is an appropriate value of the slope correction factor for the Schottky–Nordheim barrier. A typical value for $s$ is 0.95, but for simplicity we use the approximation, $s = 1$ here.

Fig. 4(b) shows the F–N plot for β-$TiO_2$/Si emitter at various separations between anode and cathode. In most cases, the FN plots exhibit two discrete sections. For low field values (right-hand side) the plot has positive slope; for high field values (left-hand side) the plot has a negative slope. Fowler–Nordheim-type equations predict that FN plots have a negative slope, so it seems highly probable that the measured low-field current is not due to cold field electron emission. Although, similar behavior was also accounted for $MoO_2$ nanostars composed of nanorods,[54] the exact cause of this low-field current is not known at present, but one possibility is that it may be some form of leakage current. The increase in the separation between cathode and anode commenced for an increase in field enhancement factor. The values of $\beta$ in high field region are estimated to be 953, 1287, 1271, and 1476 for the cathode–anode separations of 500, 1000, 1500 and 2000 μm, respectively. These values of $\beta$ for β-$TiO_2$/Si emitter are higher than that reported for amorphous and nanoparticle decorated anatase ridged $TiO_2$ nanotubes,[10] N- and Fe-doped anatase $TiO_2$ nanotubes,[9,16] rutile $TiO_2$ nanorods[14] and ZnO nanotubes.[48] To confirm the viability of the field emission measurements, particularly field enhancement factor ($\beta$) of β-$TiO_2$/Si emitters, orthodoxy text was performed using spreadsheet provided by Forbes in the ref. 55. The scaled-barrier-field ($f$) values obtained for all cathode–anode separations in β-$TiO_2$/Si emitters are shown in Table 1. The emission situation was found orthodox in all cathode–anode separations for both the lower ($f_{low}$) and highest ($f_{high}$) scaled-barrier-field values. However, the $f_{high}$ value of 0.55 obtained for the separation of 1000 μm reveals the apparently reasonable emission situation. The individual dispersion, identical smaller diameter (~10 nm), near-perfect vertical alignment, and thoroughly uniform separation between β-$TiO_2$ nanorods enhances the effective field at its top, which turns out to give enhancement of FE with better values of β and low $E_{on}$ for β-$TiO_2$/Si. For most viable use of field emitter in a variety of applications, stable FE current is one of the prerequisites. Fig. 4(c) shows the FE stability of β-$TiO_2$/Si emitters. The inset of Fig. 4(c) shows the FE image of the β-$TiO_2$. The emission current ($I$)–time ($t$) behavior recorded at preset current value of 1 μA found no obvious degradation in current within 180 min. The β-$TiO_2$/Si emitters exhibit good stability with slight current fluctuations of ±15% for average current values. This could be attributed to the excellent thermal and chemical stability of $TiO_2$.

## Conclusions

In conclusion, the large area arrays of vertically aligned 1D β-$TiO_2$ nanorods were synthesized on Si substrate utilizing simple and unique HFMVD technique. The formation of pure stoichiometric β-$TiO_2$ (*i.e.* Ti : O = 1 : 1.98) nanorods was confirmed by XRD, TEM and XPS analysis. The $E_{on}$ (at 10 μA $cm^{-2}$) of 3.9 V $\mu m^{-1}$ was observed for pristine 1D β-$TiO_2$ nanorods. The individual dispersion, identical smaller diameter, near-perfect vertically alignment, and thoroughly uniform separation between the β-$TiO_2$ nanorods direct injected electrons toward emission sites and prominently contributed to the low turn-on field, better FE characteristics and good emission stability. The β-$TiO_2$ nanorods offer strong potential for applications in FE based vacuum micro-nanoelectronic devices such

as FE displays and an intense 'point' electron sources. Moreover, the FE behavior of the pristine $TiO_2$/Si emitters may be enhanced *via* rational design of hetero-architectures.

## Acknowledgements

The authors would like to thank the Department of Science and Technology (DST), Ministry of Science and Technology of India, for INSPIRE Faculty Award No. DST/INSPIRE Faculty Award/2013/IFA13-PH-63. Authors are also thankful to Prof. Satishchandra B. Ogale, Department of Physics and Centre for Energy Science, IISER, Pune, India, for providing his expertise on this manuscript.

## References

1 R. S. Devan, R. A. Patil, J. H. Lin and Y. R. Ma, *Adv. Funct. Mater.*, 2012, **22**, 3326–3370.
2 B. Liu and E. S. Aydil, *J. Am. Chem. Soc.*, 2009, **131**, 3985–3990.
3 T. A. Kandiel, A. Feldhoff, L. Robben, R. Dillert and D. W. Bahnemann, *Chem. Mater.*, 2010, **22**, 2050–2060.
4 R. A. Patil, R. S. Devan, Y. Liou and Y. R. Ma, *Sol. Energy Mater. Sol. Cells*, 2016, **147**, 240–245.
5 R. S. Devan, Y. R. Ma, R. A. Patil and L. Schmidt-Mende, *RSC Adv.*, 2016, **6**, 62218–62225.
6 L. Kavan, M. Kalbac, M. Zukalova, I. Exnar, V. Lorenzen, R. Nesper and M. Graetzel, *Chem. Mater.*, 2004, **16**, 477–485.
7 Y. Alivov, M. Klopfer and S. Molloi, *Nanotechnology*, 2010, **21**, 505706.
8 P. G. Chavan, S. V. Shende, D. S. Joag and M. A. More, *Ultramicroscopy*, 2011, **111**, 415–420.
9 R. P. Antony, T. Mathews, K. Panda, B. Sundaravel, S. Dash and A. K. Tyagi, *J. Phys. Chem. C*, 2012, **116**, 16740–16746.
10 X. J. Xu, C. C. Tang, H. B. Zeng, T. Y. Zhai, S. Q. Zhang, H. J. Zhao, Y. Bando and D. Golberg, *ACS Appl. Mater. Interfaces*, 2011, **3**, 1352–1358.
11 J. Liang and G. M. Zhang, *ACS Appl. Mater. Interfaces*, 2012, **4**, 6053–6061.
12 J. M. Wu, H. C. Shih and W. T. Wu, *Chem. Phys. Lett.*, 2005, **413**, 490–494.
13 C. W. Wang, J. B. Chen, L. Q. Wang, Y. M. Kang, D. S. Li and F. Zhou, *Thin Solid Films*, 2012, **520**, 5036–5041.
14 H. Fu, K. Yu, H. L. Li, J. Z. Li, B. J. Guo, Y. H. Tan, C. Q. Song and Z. Q. Zhu, *Dalton Trans.*, 2015, **44**, 1664–1672.
15 H. X. Zhang, M. Zhao and Q. Jiang, *Appl. Phys. Lett.*, 2013, **103**, 023111.
16 C. C. Wang, K. W. Wang and T. P. Perng, *Appl. Phys. Lett.*, 2010, **96**, 143102.
17 L. Q. Wang, C. W. Wang, J. B. Chen, R. S. Guo, F. Zhou and W. M. Liu, *Thin Solid Films*, 2011, **519**, 8173–8177.
18 S. D. Mo and W. Y. Ching, *Phys. Rev. B: Condens. Matter Mater. Phys.*, 1995, **51**, 13023–13032.
19 M. Addamo, M. Bellardita, A. D. Paola and L. Palmisano, *Chem. Commun.*, 2006, **47**, 4943–4945.
20 T. A. Kandiel, L. Robben, A. Alkaim and D. Bahnemann, *Photochem. Photobiol. Sci.*, 2013, **12**, 602–609.
21 T. Shibata, H. Irie, M. Ohmori, A. Nakajima, T. Watanabe and K. Hashimoto, *Phys. Chem. Chem. Phys.*, 2004, **6**, 1359–1362.
22 M. Koelsch, S. Cassaignon, J. F. Guillemoles and J. P. Jolivet, *Thin Solid Films*, 2002, **403–404**, 312–319.
23 U. Diebold, *Surf. Sci. Rep.*, 2003, **48**, 53–229.
24 M. H. Yang, P. C. Chen, M. C. Tsai, T. T. Chen, I. C. Chang, H. T. Chiu and C. Y. Lee, *CrystEngComm*, 2014, **16**, 441.
25 H. Kominami, M. Kohno and Y. Kera, *J. Mater. Chem.*, 2000, **10**, 1151.
26 M. Miyauchi, H. Tokudome, Y. Toda, T. Kamiya and H. Hosono, *Appl. Phys. Lett.*, 2006, **89**, 043114.
27 W. D. Zhu, C. W. Wang, J. B. Chen, D. S. Li, F. Zhou and H. L. Zhang, *Nanotechnology*, 2012, **23**, 455204.
28 R. S. Devan, S. Y. Gao, W. D. Ho, J. H. Lin, Y. R. Ma, P. S. Patil and Y. Liou, *Appl. Phys. Lett.*, 2011, **98**, 133117.
29 R. S. Devan, W. D. Ho, J. H. Lin, S. Y. Wu, Y. R. Ma, P. C. Lee and Y. Liou, *Cryst. Growth Des.*, 2008, **8**, 4465–4468.
30 R. S. Devan, W. D. Ho, S. Y. Wu and Y. R. Ma, *J. Appl. Crystallogr.*, 2010, **43**, 498–503.
31 R. S. Devan, C. L. Lin, S. Y. Gao, C. L. Cheng, Y. Liou and Y. R. Ma, *Phys. Chem. Chem. Phys.*, 2011, **13**, 13441–13446.
32 R. A. Patil, R. S. Devan, J. H. Lin, Y. Liou and Y. R. Ma, *Sci. Rep.*, 2013, **3**, 3070.
33 J. H. Lin, R. A. Patil, M. A. Wu, L. G. Yu, K. D. Liu, W. T. Gao, R. S. Devan, C. H. Ho, Y. Liou and Y. R. Ma, *J. Mater. Chem. C*, 2014, **2**, 8667–8672.
34 D. Reyes-Coronado, G. Rodriguez-Gattorno, M. E. Espinosa-Pesqueira, C. Cab, R. deCoss and G. Oskam, *Nanotechnology*, 2008, **19**, 145605.
35 M. Choi, Z. Zhang, J. K. Chen, Z. Geng and K. Young, *RSC Adv.*, 2015, **5**, 19470–19478.
36 H. Zhou and Y. Zhang, *J. Phys. Chem. C*, 2014, **118**, 5626–5636.
37 Y. Wang, H. J. Sun, S. J. Tan, H. Feng, Z. W. Cheng, J. Zhao, A. D. Zhao, B. Wang, Y. Luo, J. L. Yang and J. G. Hou, *Nat. Commun.*, 2013, **4**, 2214.
38 M. Salari, S. H. Aboutalebi, A. T. Chidembo, I. P. Nevirkovets, K. Konstantinov and H. K. Liu, *Phys. Chem. Chem. Phys.*, 2012, **14**, 4770–4779.
39 R. S. Devan, J. H. Lin, W. D. Ho, S. Y. Wu, Y. Liou and Y. R. Ma, *J. Appl. Crystallogr.*, 2010, **43**, 1062–1067.
40 R. S. Devan, C. L. Lin, J. H. Lin, T. K. Wen, R. A. Patil and Y. R. Ma, *J. Nanosci. Nanotechnol.*, 2013, **13**, 1001–1005.
41 R. S. Devan, W. D. Ho, C. H. Chen, H. W. Shiu, C. H. Ho, C. L. Cheng, S. Y. Wu, Y. Liou and Y. R. Ma, *Nanotechnology*, 2009, **20**, 445708.
42 W. B. Hu, L. P. Li, G. S. Li, C. L. Tang and L. Sun, *Cryst. Growth Des.*, 2009, **9**, 3676–3682.
43 X. Q. Zhang, J. B. Chen, C. W. Wang, A. Z. Liao and X. F. Su, *Nanotechnology*, 2015, **26**, 175705.
44 H. Pan, X. Qiu, I. N. Ivanov, H. M. Meyer, W. Wang, W. Zhu, M. P. Paranthaman, Z. Zhang, G. Eres and B. Gu, *Appl. Catal., B*, 2009, **93**, 90–95.
45 Z. Song, H. Zhou, P. Tao, B. Y. Wang, J. Mei, H. Wang, S. G. Wen, Z. C. Song and G. J. Fang, *Mater. Lett.*, 2016, **180**, 179–183.

 

46 D. Sarkar, C. K. Ghosh and K. K. Chattopadhyay, *CrystEngComm*, 2012, **14**, 2683–2690.
47 Y. Ye, Y. H. Liu and T. L. Guo, *Surf. Coat. Technol.*, 2014, **245**, 28–33.
48 A. Wei, X. W. Sun, C. X. Xu, Z. L. Dong, M. B. Yu and W. Huang, *Appl. Phys. Lett.*, 2006, **88**, 213102.
49 C. L. Liu, H. Gao, L. Li, X. Liu, Q. Gao, H. X. Cuo, T. T. Chen and G. Q. Miao, *RSC Adv.*, 2013, **3**, 26149–26152.
50 Y. C. Chang, *RSC Adv.*, 2014, **4**, 56241–56247.
51 K. K. Naik, R. Khare, D. Chakravarty, M. A. More, R. Thapa, D. J. Late and C. S. Rout, *Appl. Phys. Lett.*, 2014, **105**, 233101.
52 T. C. Cheng, P. Y. Chen and S. Y. Wu, *Nanoscale Res. Lett.*, 2012, **7**, 125.
53 R. V. Kashid, D. J. Late, S. S. Chou, Y. K. Huang, M. De, D. S. Joag, M. A. More and V. P. Dravid, *Small*, 2013, **9**, 2730–2734.
54 A. Khademi, R. Azimirad, A. A. Zavarian and A. Z. Moshfegh, *J. Phys. Chem. C*, 2009, **113**, 19298–19304.
55 R. G. Forbes, *Proc. R. Soc. London, Ser. A*, 2013, **469**, 20130271.